Supplemental Material for

Role of virtual band population for high harmonic generation in solids

Yasuyuki Sanari[1], Hideki Hirori[1], Tomoko Aharen[1], Hirokazu Tahara[1], Yasushi Shinohara[2,3], Kenichi L. Ishikawa[2,3,4], Tomohito Otobe[5], Peiyu Xia[6], Nobuhisa Ishii[6], Jiro Itatani[6], Shunsuke A. Sato[7,8], and Yoshihiko Kanemitsu[1]

[1]*Institute for Chemical Research, Kyoto University, Uji, Kyoto 611-0011, Japan*

[2] *Photon Science Center, Graduate School of Engineering, The University of Tokyo, Bunkyo-ku, Tokyo 113-8656, Japan*

[3] *Department of Nuclear Engineering and Management, Graduate School of Engineering, The University of Tokyo, Bunkyo-ku, Tokyo 113-8656, Japan*

[4] *Research Institute for Photon Science and Laser Technology, The University of Tokyo, 7-3-1 Hongo, Bunkyo-ku, Tokyo 113-0033, Japan*

[5]*Kansai Photon Science Institute, National Institutes for Quantum and Radiological Science and Technology, Kizugawa, Kyoto 619-0615, Japan*

[6]*Institute for Solid State Physics, The University of Tokyo, Kashiwa, Chiba 277-8581, Japan*

[7]*Center for Computational Sciences, University of Tsukuba, Tsukuba 305-8577, Japan*

[8]*Max Planck Institute for the Structure and Dynamics of Matter, Luruper Chaussee 149, 22761 Hamburg, Germany*

I. Synthesis of lead halide perovskite sample

The single crystals used in this study were prepared by the antisolvent vapor assisted crystallization method. MACl(1 mmol, Tokyo Chemical Industry Co. Ltd) and $PbCl_2$(1 mmol, anhydrous, Sigma Aldrich) were first dissolved in 1mL of dimethyl sulfoxide (FUJIFILM Wako Pure Chemical Corporation), then 1mL of N,N-dimethylformamide (Tokyo Chemical Industry Co. Ltd.) was added to the resulting solution. A small vial partially filled with this perovskite precursor solution was placed in a bigger vial containing Toluene. The lid for this bigger vial is closed tightly for vapor diffusion. The crystals of $MAPbCl_3$ normally are obtained within a few days.

II. HHG measurement

The HHG experiments used mid-infrared (MIR) pulses at 3.5 μm (0.35 eV) from a KTA-based optical parametric amplifier. The MIR pulses were compressed by spectral broadening in a germanium plate followed by dispersion compensation in sapphire and fused silica plates. The pulse duration was measured to be 60 fs by second harmonic generation frequency-resolved optical gating (SHG-FROG). The harmonic yields as a function of the peak electric field or the crystallographic orientation angle were measured by rotating the variable neutral density filter or half-waveplate. The harmonics generated in and transmitted through the sample were measured with a charge-coupled-device camera sensitive to the visible and ultraviolet regions and an InGaAs array detector sensitive to the near-infrared region.

III. Theoretical method

We perform time-evolution of density-matrix, calling TD-DM, relying on time-dependent one-body Hamiltonian based on the velocity gauge:

$$i\hbar\frac{\mathrm{d}}{\mathrm{d}t}\rho = [h(t),\rho] + s, \qquad h\ (t) = h_0 + \frac{1}{m}\boldsymbol{p}\cdot\boldsymbol{A}(t) + \frac{1}{2m}\boldsymbol{A}^2(t) + \Sigma(t), \qquad (1)$$

where h_0, $\boldsymbol{p}$, $\boldsymbol{A}$, Σ, and s are the field-free Hamiltonian, the momentum operator, the vector potential, the scissors operator for correcting gap, and the collision term accounting for the interband relaxation. In the actual calculation, taking matrix elements of both sides of the equation with a basis set leads to the working equation. We employ orbitals derived from density-functional theory with local-density approximation (DFT-LDA) [S1,S2], and corresponding matrix elements are chosen as

$$\langle\phi_{b\boldsymbol{k}}|h_0|\phi_{c\boldsymbol{k}}\rangle = \epsilon_{b\boldsymbol{k}}\delta_{bc},\ \langle\phi_{b\boldsymbol{k}}|\boldsymbol{p}|\phi_{c\boldsymbol{k}}\rangle = \boldsymbol{p}^{\boldsymbol{k}}_{bc},\ \rho^{\boldsymbol{k}}_{bc}(t) = \langle\phi_{b\boldsymbol{k}}|\rho(t)|\phi_{c\boldsymbol{k}}\rangle, \qquad (2)$$

where $\epsilon_{b\boldsymbol{k}}$ and $\boldsymbol{p}^{\boldsymbol{k}}_{bc}$ are an eigenvalue and a momentum operator matrix element derived by DFT-LDA. Band gaps derived from DFT-LDA is usually underestimated compared to values of more sophisticated theories and experimental values. Then, we introduced the scissors operator to let the gap widen. To investigate the effect on interband relaxation against nonlinear absorption, we introduce the scattering term into (1).

III-1. Intraband and interband decomposition of the induced current

Let us introduce a basis set to define a diagonal and an off-diagonal component of our density matrix. The basis set is denoted as $\varphi_{\alpha\mathrm{k}}$. The diagonal and the off-diagonal components are $\alpha = \beta$ and $\alpha \neq \beta$ for $\tilde{\rho}^{\boldsymbol{k}}_{\alpha\beta}(t) = \langle\varphi_{\alpha\boldsymbol{k}}|\rho(t)|\varphi_{\beta\boldsymbol{k}}\rangle$. Any observable, $O(t) = \mathrm{tr}(\rho o)$, can be decomposed to diagonal and off-diagonal components according to the density-matrix as

$$O(t) = \sum_{\alpha\beta\boldsymbol{k}} \tilde{\rho}^{\boldsymbol{k}}_{\alpha\beta}\tilde{o}^{\boldsymbol{k}}_{\beta\alpha} = \sum_{\alpha\boldsymbol{k}} \tilde{\rho}^{\boldsymbol{k}}_{\alpha\alpha}\tilde{o}^{\boldsymbol{k}}_{\alpha\alpha} + \sum_{\alpha\beta(\alpha\neq\beta)\boldsymbol{k}} \tilde{\rho}^{\boldsymbol{k}}_{\alpha\beta}\tilde{o}^{\boldsymbol{k}}_{\beta\alpha} \equiv O_{\mathrm{D}}(t) + O_{\mathrm{OD}}(t). \quad (3)$$

A proper physical picture must be introduced for the choice of the basis set. A physically reasonable way is that instantaneous eigenfunction of the time-dependent Hamiltonian:

$$h(t)\varphi^{(t)}_{\alpha\boldsymbol{k}} = \varepsilon^{(t)}_{\alpha\boldsymbol{k}}\varphi^{(t)}_{\alpha\boldsymbol{k}} \quad (4)$$

where superscript (t) means that this function and value parametrically depend on time, namely we do not impose any relation between different times, $\left(\varepsilon^{(t)}_{\alpha\boldsymbol{k}}, \varphi^{(t)}_{\alpha\boldsymbol{k}}\right)$ and $\left(\varepsilon^{(t')}_{\alpha\boldsymbol{k}}, \varphi^{(t')}_{\alpha\boldsymbol{k}}\right)$. To think about the physics behind the choice, let us argue an adiabatic situation under a slowly varying field. Under the slowly varying field, the system does not undergo any excitation guaranteed by the adiabatic theorem. For the lattice periodic part of the orbital function, we have an equation of motion:

$$i\hbar\frac{\mathrm{d}}{\mathrm{d}t}u_{b\boldsymbol{k}} = h_{\boldsymbol{k}}(t)u_{b\boldsymbol{k}}, h_{\boldsymbol{k}}(t) = h_{0,\boldsymbol{k}} + \frac{1}{m}\boldsymbol{p}\cdot\left(\boldsymbol{k}+\boldsymbol{A}(t)\right) + \frac{1}{2m}\left(\boldsymbol{k}+\boldsymbol{A}(t)\right)^2 + \Sigma_{\boldsymbol{k}}(t),$$
$$\psi_{b\boldsymbol{k}}(\boldsymbol{r},t) = e^{i\boldsymbol{k}\cdot\boldsymbol{r}}u_{b\boldsymbol{k}}(\boldsymbol{r},t) \quad (5)$$

which is equivalent to Eq. (1). Since the time dependence in the Hamiltonian appears time-dependent momentum shift via the vector potential $h_{\boldsymbol{k}}(t) = h_{\boldsymbol{k}+\boldsymbol{A}(t)}$, the adiabatic limit of the wave function is $u^{\mathrm{adiabatic}}_{b\boldsymbol{k}} \propto v_{b\boldsymbol{k}+\boldsymbol{A}(t)}$, $h_{\boldsymbol{k}+\boldsymbol{A}(t)}v_{b\boldsymbol{k}+\boldsymbol{A}(t)} = \varepsilon_{b\boldsymbol{k}+\boldsymbol{A}(t)}v_{b\boldsymbol{k}+\boldsymbol{A}(t)}$ if energy eigenvalues do not face crossing each other. The adiabatic wave function is nothing but the eigenfunction of instantaneous Hamiltonian.

We further discuss the reason why this choice that the adiabatic basis is reasonable. We are interested in the induced current as an observable:

$$\boldsymbol{J}(t) = \boldsymbol{J}_{\mathrm{intra}}(t) + \boldsymbol{J}_{\mathrm{inter}}(t),$$
$$\boldsymbol{J}_{\mathrm{intra}}(t) = -\frac{e}{\Omega m}\sum_{\alpha\boldsymbol{k}}\tilde{\rho}^{\boldsymbol{k}}_{\alpha\alpha}(t)\left(\tilde{\boldsymbol{p}}^{\boldsymbol{k},(t)}_{\alpha\alpha} + \boldsymbol{A}(t)\right), \boldsymbol{J}_{\mathrm{inter}}(t) = -\frac{e}{\Omega m}\sum_{\alpha\beta(\alpha\neq\beta)\boldsymbol{k}}\tilde{\rho}^{\boldsymbol{k}}_{\alpha\beta}(t)\tilde{\boldsymbol{p}}^{\boldsymbol{k},(t)}_{\beta\alpha} \quad (6)$$

where $e(>0)$, Ω, and m, are the electron charge, volume of crystal, and mass of electron. Intraband and interband current densities are defined as the diagonal and the off-diagonal component in Eq. (3). The superscript (t) of the momentum operator represents the parametric time dependence on time as in the adiabatic wave function. Let us concentrate on the intraband contribution because this is the dominant term in our simulation results. The momentum operator diagonal component has the following relation: $\boldsymbol{p}^{\boldsymbol{k}}_{\alpha\alpha} = \partial\varepsilon_{\alpha\boldsymbol{k}}/\partial\boldsymbol{k}$, namely just group velocity derived from the band dispersion. Therefore, the intraband current can be summarized as

$$\boldsymbol{J}_{\text{intra}}(\boldsymbol{t}) = -\frac{e}{\Omega m}\sum_{\alpha\boldsymbol{k}} n_{\alpha\boldsymbol{k}}(t)\left(\frac{\partial \varepsilon_{\alpha\boldsymbol{k}}}{\partial \boldsymbol{k}}\right)_{\boldsymbol{k}+\boldsymbol{A}(t)}, n_{\alpha\boldsymbol{k}}(t) = \tilde{\rho}^{\boldsymbol{k}}_{\alpha\alpha}(t). \quad (7)$$

The first term is interpreted as population times group velocity, invoking intraband current in which the population is sometimes regarded as time-independent constant. While anharmonicity of the band dispersion is the source of high-order harmonics (HH), the population is the source as well. The former aspect is totally determined by a band dispersion and the acceleration theorem, $\mathrm{d}\boldsymbol{k}/\mathrm{d}t = \mathrm{d}\boldsymbol{A}/\mathrm{d}t$. Later aspect is somewhat thought of as transient excitation amount due to the electric field reflecting the orientation dependence of driving field polarization.

III-2. Band averaged intraband current

To get more insight from the detail of intraband current formula, Eq. (7), we decompose the total to band-by-band contribution. By looking at the band structure in Fig. 3(a), many crossing points in the valence bands (VBs), the group of 9 energy bands at topmost energy among valence bands composed by s-nature orbitals of Pb and p-nature orbitals Cl atoms. The band crossing leads to a breakdown of adiabatic discussion within a single-band picture. When we think of a single band treatment, the population jump into another band happens when a crystal momentum $\boldsymbol{k}(t) = \boldsymbol{k}(t=0) + \boldsymbol{A}(t)$ passes through the crossing point leading to unphysical sharp stepwise time dependence. This single-band intraband current shows much larger high harmonic components due to the sharp structure from the unphysical reason. To overcome this failure, we introduce a band averaged intraband current collecting multi-band intraband current components over a particular range such that bands, as a group, are isolated energetically from other band groups, *e.g.* VBA. By the multi-band averaging, the sharp jump of a population is significantly canceled by the counter sharp jump.

We define the band averaged intraband current density over VBs as

$$\boldsymbol{J}_{\text{VBs}}(t) = -\frac{e}{\Omega m}\sum_{\alpha(\in\text{VBs})\boldsymbol{k}} [n_{\alpha\boldsymbol{k}}(t) - n_{\alpha\boldsymbol{k}}(t=0)]\left\langle \varphi^{(t)}_{\alpha\boldsymbol{k}}\middle|\boldsymbol{p} + \boldsymbol{A}(t)\middle|\varphi^{(t)}_{\alpha\boldsymbol{k}}\right\rangle,$$
$$n_{\alpha\boldsymbol{k}}(t) = \left\langle \varphi^{(t)}_{\alpha\boldsymbol{k}}\middle|\rho(t)\middle|\varphi^{(t)}_{\alpha\boldsymbol{k}}\right\rangle. \quad (8)$$

Note that the detailed description of the population, $n_{bk}(t)$, will be discussed in Section IV. The subtraction of the initial population, $n_{\alpha\boldsymbol{k}}(t=0)$, is introduced to discuss population change from the ground state. The contribution from this term is ideally zero for when we have infinite Hilbert space for each $\boldsymbol{k}$ and infinite number for the Brillouin zone sampling because the valence bands are initially fully occupied and do not have any

current. The band averaged intraband current for VBs shows much smoother behavior and is well coincide with the total intraband current as shown in Fig. S1. The band-averaged population of VBs is similarly defined as

$$\Delta n_{\mathrm{VBs}} = \frac{1}{\Omega} \sum_{\alpha(\in \mathrm{VBs})k} [n_{\alpha k}(t) - n_{\alpha k}(t=0)]\,. \tag{9}$$

III-3. Numerical scheme to evaluate velocity from the band averaged current density and population

A velocity derived by the band averaged current density and population is defined by $J_{\mathrm{VBs}}(t) = e\Delta n_{\mathrm{VBs}}(t) V_{\mathrm{VBs}}(t)$. This velocity can be interpreted as an averaged velocity over VBs. When we numerically evaluate the velocity, the denomination of the time-dependent population appears. The time-dependent population could be very tiny for weak-field, especially at the very beginning of the simulation, leading to numerical instability. To avoid instability, we introduce a window function in the time domain such that extracting values around the strong field. Precisely, we use a Gaussian function for the window as,

$$\tilde{V}_{\mathrm{VBs}}(t) = \frac{J_{\mathrm{VBs}}(t)}{\Delta n_{\mathrm{VBs}}(t) - 2.0 \times 10^{-18}} e^{-(t-T/2)^2/u^2}, \tag{10}$$

where T =400 fs and u = 20 fs. Fourier transforms of this velocity is shown in Fig. 5.

III-4. Interband relaxation within the velocity gauge

The interband relaxation is usually introduced for a field-free system, to imitate that interband polarization decoherence due to interactions among electrons and to other subsystems such as phonon. The DM of the system undergoes diagonal via the relaxation. The diagonal and off-diagonal components depend on the choice of representation for DM. Usually, eigenfunctions of the one-body Hamiltonian are employed for representation. The choice of the representation becomes ambiguous when the external field is. We employ the instantaneous eigenfunction of the time-dependent Hamiltonian based on the velocity-gauge in Eq. (4). According to the adiabatic theorem, no interband relaxation happens with this representation.

The explicit expression of the relaxation term is

$$s = -i \sum_{\alpha\beta(\alpha\neq\beta)\boldsymbol{k}} \frac{1}{\tau} \left|\varphi_{\alpha\boldsymbol{k}}^{(t)}\right\rangle \left\langle\varphi_{\alpha\boldsymbol{k}}^{(t)}\right|, \tag{11}$$

where τ is the relaxation constant.

III-5. Numerical dimension of the simulation

Before time-dependent simulation of Eq. (1), we perform DFT-LDA calculation for $CsPbCl_3$ crystal using the Elk code [S3]. The lattice constant is chosen as 0.561 nm [S4], experimental value for the crystal. The localize orbital is included in the DFT-LDA calculation. The number of empty bands is 81, *i.e.* totally 108 bands including the valence bands, spanning 98.5 eV energy range. The number of *k*-grid in the first-Brillouin zone is 32^3 without symmetry restriction for the time-dependent simulation. The momentum operator matrix elements evaluated with the DFT-LDA Kohn-Sham orbital are provided by also the Elk code, written in PMAT.OUT on the disk. The DFT-LDA calculation with the finite Brillouin zone sampling predicts 1.79 eV at the R-point.

For the electron dynamics simulation, we use 1.25 eV gap correction to obtain 3.04 eV bandgap by using the scissors operator. The time-step is 24 as, 1.0 a.u. We use an applied electric field shape:

$$A(t) = \frac{E_0}{\omega}\sin^4\left(\frac{\pi t}{T}\right)\sin\left(\omega\left(t-\frac{T}{2}\right)\right) \quad (0 \le t < T), \qquad E(t) = -\dot{A}, \tag{12}$$

where E_0, ω, and T are maximum electric field strength, angular frequency of the electric field, and pulse duration parameter. We employ $\hbar\omega = 0.34$ eV and $T = 400$ fs in which the full width at half maximum of the envelope square is 104 fs. We integrate *k*-dependent expectation value over the entire first-Brillouin zone, not only a direction, to evaluate the values, the current densities and the population.

IV. Evaluation of temporal population dynamics

Here, we revisit the derivation of the transient population, $n_{a\boldsymbol{k}}(t)$, in Eq. (8) based on the many-body wavefunction. For this purpose, we first define the many-body ground state of a semiconductor with the independent particle approximation. For simplicity, we assume that electrons occupy only a single valence band. The corresponding ground state is described by the following Slater determinant,

$$\Phi_0(\boldsymbol{r}_1,\cdots,\boldsymbol{r}_N) = \frac{1}{\sqrt{N!}}\begin{bmatrix} e^{i\boldsymbol{k}_1\cdot\boldsymbol{r}_1}u^0_{v\boldsymbol{k}_1}(\boldsymbol{r}_1) & \cdots & e^{i\boldsymbol{k}_N\cdot\boldsymbol{r}_1}u^0_{v\boldsymbol{k}_N}(\boldsymbol{r}_1) \\ \vdots & \ddots & \vdots \\ e^{i\boldsymbol{k}_1\cdot\boldsymbol{r}_N}u^0_{v\boldsymbol{k}_1}(\boldsymbol{r}_N) & \cdots & e^{i\boldsymbol{k}_N\cdot B_N}u^0_{v\boldsymbol{k}_N}(\boldsymbol{r}_N) \end{bmatrix}, \tag{13}$$

where the ground-state Bloch orbitals, $u^0_{v\boldsymbol{k}}(\boldsymbol{r})$, with the Bloch wavevector, $\boldsymbol{k}$, satisfy the following single-particle Schrödinger equation

$$h(t=-\infty)u^0_{v\boldsymbol{k}}(\boldsymbol{r}) = \varepsilon^0_{v\boldsymbol{k}}u^0_{v\boldsymbol{k}}(\boldsymbol{r}), \tag{14}$$

with the Hamiltonian of Eq. (5). Likewise, the time-dependent many-body wavefunction of the system is given by

$$\Psi(\boldsymbol{r}_1,\cdots,\boldsymbol{r}_N,t)=\frac{1}{\sqrt{N!}}\begin{bmatrix} e^{i\{\boldsymbol{k}_1+\boldsymbol{A}(t)\}\cdot\boldsymbol{r}_1}u_{v\boldsymbol{k}_1}(\boldsymbol{r}_1,t) & \cdots & e^{i\{\boldsymbol{k}_N+\boldsymbol{A}(t)\}\cdot\boldsymbol{r}_1}u_{v\boldsymbol{k}_N}(\boldsymbol{r}_N,t) \\ \vdots & \ddots & \vdots \\ e^{i\{\boldsymbol{k}_1+\boldsymbol{A}(t)\}\cdot\boldsymbol{r}_N}u_{v\boldsymbol{k}_1}(\boldsymbol{r}_N,t) & \cdots & e^{i\{\boldsymbol{k}_N+\boldsymbol{A}(t)\}\cdot\boldsymbol{r}_N}u_{v\boldsymbol{k}_N}(\boldsymbol{r}_N,t) \end{bmatrix}, \quad (15)$$

where the time-dependent Bloch orbitals, $u_{v\boldsymbol{k}}(\boldsymbol{r},t)$, satisfy the single-particle Schrödinger equation, Eq. (5).

To evaluate the state population, we then introduce a single particle-hole state with the bracket notation as

$$|\Phi_{vc,\boldsymbol{k}_1}\rangle=\hat{a}^{\dagger}_{c\boldsymbol{k}_1}\hat{a}_{v\boldsymbol{k}_1}\ |\Phi_0\rangle, \quad (16)$$

where $|\Phi_0\rangle$ is the ket vector of the ground state wavefunction, Eq. (13), $\hat{a}^{\dagger}_{c\boldsymbol{k}}$ is the creation operator for a conduction state at $\boldsymbol{k}$, and $\hat{a}_{v\boldsymbol{k}}$ is the annihilation operator of the valence state. In the Slater determinant expression, $|\Phi_{vc,\boldsymbol{k}_1}\rangle$ is described as

$$\Phi_{vc,\boldsymbol{k}_1}(\boldsymbol{r}_1,\cdots,\boldsymbol{r}_N)=\frac{1}{\sqrt{N!}}\begin{bmatrix} e^{i\boldsymbol{k}_1\cdot\boldsymbol{r}_1}u^0_{c\boldsymbol{k}_1}(\boldsymbol{r}_1) & \cdots & e^{i\boldsymbol{k}_N\cdot\boldsymbol{r}_1}u^0_{v\boldsymbol{k}_N}(\boldsymbol{r}_1) \\ \vdots & \ddots & \vdots \\ e^{i\boldsymbol{k}_1\cdot\boldsymbol{r}_N}u^0_{c\boldsymbol{k}_1}(\boldsymbol{r}_N) & \cdots & e^{i\boldsymbol{k}_N\cdot\boldsymbol{r}_N}u^0_{v\boldsymbol{k}_N}(\boldsymbol{r}_N) \end{bmatrix}. \quad (17)$$

The temporal population of the single particle-hole state can be evaluated as

$$\left|\langle\Phi_{vc,\boldsymbol{k}_1}|\Psi(\mathrm{t})\rangle\right|^2=\langle\Psi(\mathrm{t})|\hat{a}^{\dagger}_{c\boldsymbol{k}_1}\hat{a}_{v\boldsymbol{k}_1}\ |\Phi_0\rangle\langle\Phi_0|\hat{a}^{\dagger}_{v\boldsymbol{k}_1}\hat{a}_{c\boldsymbol{k}_1}|\Psi(\mathrm{t})\rangle\ , \quad (18)$$

where $|\Psi(t)\rangle$ is the ket vector of the time-dependent many-body state in Eq. (15). Thanks to the plane wave modulation of the Bloch orbitals, $e^{i\boldsymbol{k}\cdot\boldsymbol{r}}$, in the fine Brillouin zone sampling limit ($N\to\infty$), the population of the single particle-hole state, Eq. (18), can be evaluated as

$$\left|\langle\Phi_{vc,\boldsymbol{k}_1}|\Psi(\mathrm{t})\rangle\right|^2=\left|\langle u^0_{c\boldsymbol{k}_1}|u_{v,\boldsymbol{k}_1-\boldsymbol{A}(t)}(t)\rangle\right|^2 \times\left|\langle u^0_{v\boldsymbol{k}_2}|u_{v,\boldsymbol{k}_2-\boldsymbol{A}(t)}(t)\rangle\right|^2\times\cdots\times\left|\langle u^0_{v\boldsymbol{k}_N}|u_{v,\boldsymbol{k}_N-\boldsymbol{A}(t)}(t)\rangle\right|^2\ . \quad (19)$$

Here, we note that the overlap between the two Bloch orbitals with the wavevector shift, $\boldsymbol{k}$ and $\boldsymbol{k}-\boldsymbol{A}(t)$, are naturally introduced as a consequence of the overlap of the many-body wavefunctions. Employing a similar procedure in Eq. (18) and Eq. (19), one can further evaluate the population of a conduction state at $\boldsymbol{k}$ with the number operator $\hat{n}_{c\boldsymbol{k}}=\hat{a}^{\dagger}_{c\boldsymbol{k}}\hat{a}_{c\boldsymbol{k}}$ by

$$n_{c\boldsymbol{k}}(t)=\langle\Psi(\mathrm{t})|\hat{n}_{c\boldsymbol{k}}|\Psi(\mathrm{t})\rangle=\left|\langle u^0_{c\boldsymbol{k}}|u_{v,\boldsymbol{k}-\boldsymbol{A}(t)}(t)\rangle\right|^2\ . \quad (20)$$

By changing the label, we obtain

$$n_{c\boldsymbol{k}+\boldsymbol{A}(t)}(t)=\langle\Psi(\mathrm{t})|\hat{n}_{c\boldsymbol{k}+\boldsymbol{A}(t)}|\Psi(\mathrm{t})\rangle=\left|\langle u^0_{c\boldsymbol{k}+\boldsymbol{A}(t)}|u_{v,\boldsymbol{k}}(t)\rangle\right|^2\ . \quad (21)$$

Thus, the temporal population can be evaluated by the overlap of the time-dependent

single-particle orbital and the wavenumber-shifted ground-state Bloch orbital.

V. Decomposition of calculated HHG spectra

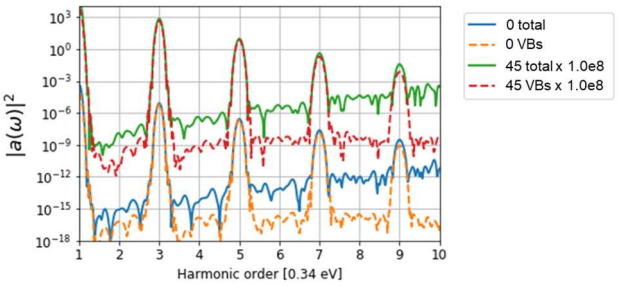

Fig. S1. Decomposition of the harmonic spectra calculated with a peak electric field E = 10 MV/cm. Solid lines for the total HHG spectra of 0 (blue) and 45 degrees (green), and dashed lines for those from VBs of 0 (red) and 45 degrees (orange). The spectra of VBs closely dominate the total HHG for the both angle cases.

VI. Rabi oscillation and virtual population dynamics

Here, we revisit the Rabi oscillation and virtual population dynamics with a simple two-level model. The dynamics of the two-level system is described by the time-dependent Schrödinger equation

$$\mathrm{i}\hbar\frac{\partial}{\partial \mathrm{t}}|\psi(t)\rangle = H(t)|\psi(t)\rangle \tag{22},$$

with the following two-by-two Hamiltonian matrix

$$H(t) = \frac{\Delta}{2}\begin{pmatrix}1 & 0\\ 0 & -1\end{pmatrix} + \begin{pmatrix}0 & E(t)\\ E(t) & 0\end{pmatrix} \tag{23},$$

where Δ is the energy gap of the two-level system, and $E(t)$ is an external electric field. For simplicity, we consider the following sinusoidal form for the electric field, $E(t) = E_0\sin(\omega t)$, where E_0 is the amplitude of the electric field, and ω is its frequency. To investigate the population dynamics, we numerically solve the Schrödinger equation (9) by setting the initial wavefunction to the ground state, $|\psi(t=0)\rangle = |g\rangle = (0,1)^T$. Here, we evaluate the dynamics of the population of the excited state, $|e\rangle = (1,0)^T$, as $\rho_e(t) = |\langle\psi(t)|e\rangle|^2$.

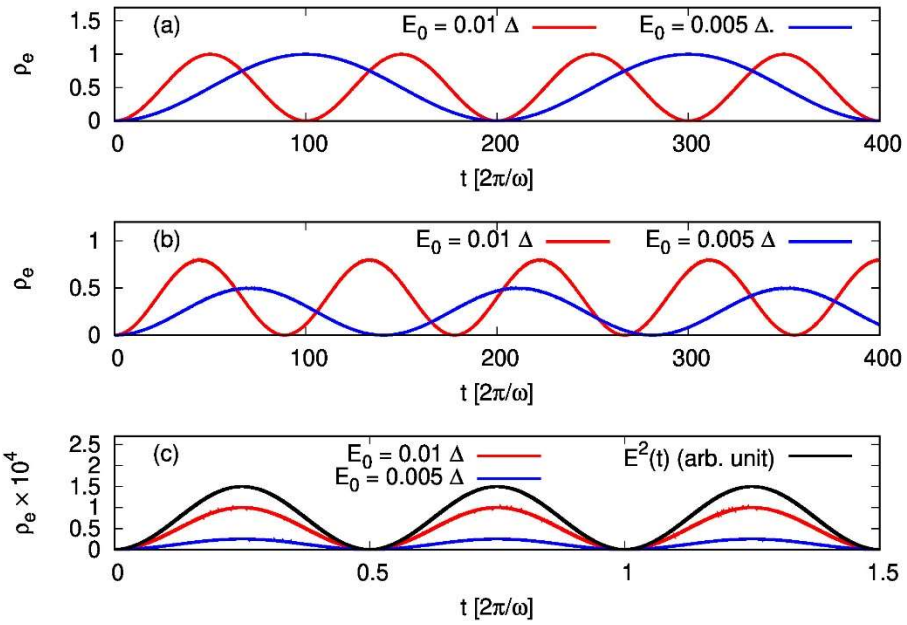

Fig. S2. Computed population dynamics of the two-level model as a function of time in (a) the resonant regime $\omega = \Delta/\hbar$, (b) the slightly off-resonant retime $\omega = 0.995\Delta/\hbar$, and (c) the deeply off-resonant regime $\omega = 0.001\Delta/\hbar$.

First, we investigate the population dynamics in the resonant regime by setting $\omega = \Delta/\hbar$. Figure S2 (a) shows the computed population $\rho_e(t)$ as a function of time in the resonant regime. Note that the time-axis is described in the unit of the optical-cycle. The population dynamics is computed with two different amplitudes of the electric field, E_0. Both results show the population oscillation under the continuous driving. During the oscillation, the population reaches one and returns to zero. This oscillatory behavior is known as Rabi oscillation, and the frequency of Rabi oscillation is given by $\Omega_R = E_0/\hbar$. The evaluated Rabi cycle, $2\pi/\Omega_R$, is one hundred optical cycles for the field strength E_0 of 0.01Δ (red line), and it is two hundred optical cycles for $E_0 = 0.005\Delta$ (blue line). As seen from Fig. S2 (a), these evaluated Rabi cycles are consistent with the numerical results.

Next, we investigate the population dynamics in a slightly off-resonant regime by setting $\omega = 0.995\Delta/\hbar$. Figure S2 (b) shows the computed population dynamics in the slightly off-resonant regime. The computed population shows the similar oscillatory behavior to the Rabi oscillation shown in Fig. S2 (a). However, the frequency of the oscillation is detuned, and the population does not reach to one anymore. This feature is known as the off-resonant Rabi oscillation.

Finally, we investigate the population dynamics in a deeply off-resonant regime by

setting $\omega = 0.001\Delta/\hbar$. Figure S2 (c) shows the computed population dynamics in the deeply off-resonant regime with different electric field amplitudes E_0; 0.01Δ (red line) and 0.05Δ (blue line). The black line shows the square of the applied electric field $E^2(t)$. Although the population dynamics shows an oscillatory behavior, it is qualitatively different from the Rabi oscillation in Fig. S2 (a) or the off-resonant Rabi oscillation in Fig. S2 (b): the amplitude of the population oscillation in the strongly off-resonant regime is tiny while the substantial amount of the population is transferred to the excited state in the resonant and off-resonant Rabi regimes. Furthermore, the cycle of the oscillation in the strongly off-resonant regime does not depend on the field strength and is half of the optical cycle although the (detuned) Rabi cycle significantly depends on the field strength and is much longer than the optical cycle for the present field strength. Importantly, we note that the population dynamics (quasi)-adiabatically follows the instantaneous field strength in the deeply off-resonant regime. Therefore, the excited population can exist only during the field driving, and it returns to zero after the driving as shown in Fig. 4 (e) in the main text. In this sense, the excited population in the off-resonant regime is not *real* but *virtual* as it disappears after the field driving. We shall call such population *virtual population* in order to clearly distinguish it from *real population* appearing in the (off-resonant) Rabi oscillation.

VI. Anisotropy of virtual population and high-order harmonic generation

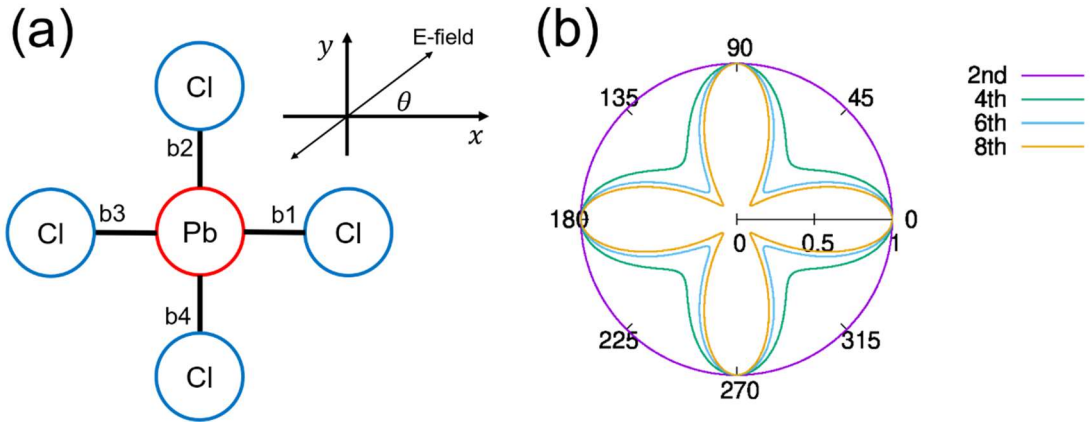

Fig. S3. (a) Schematics of chemical bonding in $MAPbCl_3$ crystal for the calculation. (b) Calculated angular dependence of virtual population for different harmonic orders.

Here, we elucidate the microscopic mechanism of the anisotropy of virtual population

dynamics on different harmonic orders, as shown in Fig. 4 in the main text. Due to the strong electronegativity of Cl, Cl ions attract electrons from Pb, and thus the chemical bond may have strong directivity. Based on this directivity of chemical bonds, we develop a simple model to describe the anisotropy of virtual population dynamics, which is responsible for the high-order harmonic generation in $MAPbCl_3$ crystal. To construct a model, we consider the configuration as described in Fig. S3 (a). We expect that the chemical bonds, which are denoted as b1, b2, b3, and b4 in Fig. S3, have the strong directivity. Based on the strong directivity, we further assume that the horizontal bonds (b1 and b3) respond to only the *x*-component of applied electric fields, E_x, while the vertical bonds (b2 and b4) respond to only the *y*-component, E_y. Thus, the x-component of electric fields induces the virtual population only on b1 and b3 bonds while the y-component of electric fields induces the virtual population only on b2 and b4 bonds:

$$n_{b1} = n_{b3} = n[E_x] = n[E_0 \cos\theta], \qquad n_{b2} = b_{b4} = n\big[E_y\big] = n[E_0 \sin\theta] \tag{24}.$$

For simplicity, we assume that *n*-th order harmonics of the virtual population is proportional to *n*-th order electric fields as

$$n_{b1}^{(n)} = n_{b3}^{(n)} = n^{(n)}[E_x] \propto E_x^n = E_0^n \cos^n\theta \tag{25},$$

$$n_{b2}^{(n)} = n_{b4}^{(n)} = n^{(n)}\big[E_y\big] \propto E_y^n = E_0^n \sin^n\theta \tag{26}.$$

By summing the contributions from all the bonds (b1, b2, b3, and b4), the *n*-th order harmonics of the virtual population can be evaluated as

$$n^{(n)}(\theta) \propto E^n[\cos^n\theta + \sin^n\theta] \tag{27}.$$

Note that, as discussed in the main text, only even order harmonic components exist because of the spatial inversion symmetry. Figure S3 (b) shows the angle dependence of the virtual population on each harmonic order. The results are computed with Eq. (27) and are normalized at $0°$. One sees that the second order harmonics (purple line) has the circular symmetry, and the signal intensities at $0°$ and $45°$ are identical. In contrast, the 4th, 6th, and 8th order harmonics show the strong reduction of the signal intensity at $45°$. The signal intensity reduction becomes more significant in higher order harmonics. This behavior is consistent with that of the virtual population in Fig. 4 of the main text. Furthermore, the overall angular dependence of the simple model in Fig. S3 (b) is qualitatively consistent with the angular dependence of the high order harmonic generation shown in Fig. 2 of the main text. This fact indicates that the strong directivity of chemical bonds in $MAPbCl_3$ plays an important role in the characteristic angular dependence of the high-order harmonic generation from perovskites.

References

[S1] P. Hohenber and W. Kohn, Phys. Rev. **136**, B864 (1964).

[S2] John P. Perdew and Yue Wang, Phys. Rev. B **45**, 13244 (1992).

[S3] http://elk.sourceforge.net/

[S4] Chr. Kn. Møller, Nature **182**, 1436 (1958).